

Assessment of 226Ra and U colloidal transport in a mining environment

Reymond, Marine; Descostes, Michaël; Besançon, Clémence; Leermakers, Martine; Billon, Sophie; Cherfallot, Gaël; Muguet, Marie; Beaucaire, Catherine; Smolíková, Vendula; Patrier, Patricia

Published in:
Chemosphere

DOI:
[10.1016/j.chemosphere.2023.139497](https://doi.org/10.1016/j.chemosphere.2023.139497)

Publication date:
2023

License:
CC BY-NC-ND

Document Version:
Accepted author manuscript

[Link to publication](#)

Citation for published version (APA):

Reymond, M., Descostes, M., Besançon, C., Leermakers, M., Billon, S., Cherfallot, G., Muguet, M., Beaucaire, C., Smolíková, V., & Patrier, P. (2023). Assessment of 226Ra and U colloidal transport in a mining environment. *Chemosphere*, 338, Article 139497. <https://doi.org/10.1016/j.chemosphere.2023.139497>

Copyright

No part of this publication may be reproduced or transmitted in any form, without the prior written permission of the author(s) or other rights holders to whom publication rights have been transferred, unless permitted by a license attached to the publication (a Creative Commons license or other), or unless exceptions to copyright law apply.

Take down policy

If you believe that this document infringes your copyright or other rights, please contact openaccess@vub.be, with details of the nature of the infringement. We will investigate the claim and if justified, we will take the appropriate steps.

1 **Assessment of ²²⁶Ra and U colloidal transport in a mining environment**

2 Marine Reymond^a; Michael Descostes^{b,c}; Clémence Besancon^{b,*}; Martine Leermakers^d;
3 Sophie Billon^a; Gaël Cherfallot^a; Marie Muguet^{b,#}; Catherine Beaucaire^e; Vendula
4 Smolikova^d; Patricia Patrier^a.

5
6 ^a Institut de Chimie des Milieux et des Matériaux de Poitiers (IC2MP), UMR 7285, Université
7 de Poitiers, CNRS, HydrASA, F-86073 Poitiers, France;

8 ^b Orano Environmental R&D Dpt, 125 avenue de Paris, 92320, Châtillon, France

9 ^c Centre de Géosciences, MINES Paris, PSL University, 35 rue St Honoré, 77300
10 Fontainebleau, France

11 ^d Analytical, Environmental & Geo-Chemistry (AMGC), Vrije Universiteit Brussels (VUB),
12 Pleinlaan 2, 1050 Brussels, Belgium

13 ^e Consultant, 21540 Chevannay, France

14
15 *: corresponding coauthor

16 clemence.besancon@orano.group; +33 (0)1 34 96 05 14

17
18 #: present address

19 muguet.marie@aesn.fr

25 **Highlights**

- 26 • An innovative approach was developed to assess the colloidal transport of ^{226}Ra and
27 U
- 28 • Water sampling, DGT, and solid characterization were combined with geochemical
29 modelling
- 30 • ^{226}Ra colloidal transport is explained by coprecipitation into barite
- 31 • This approach can be applied to other trace elements

32

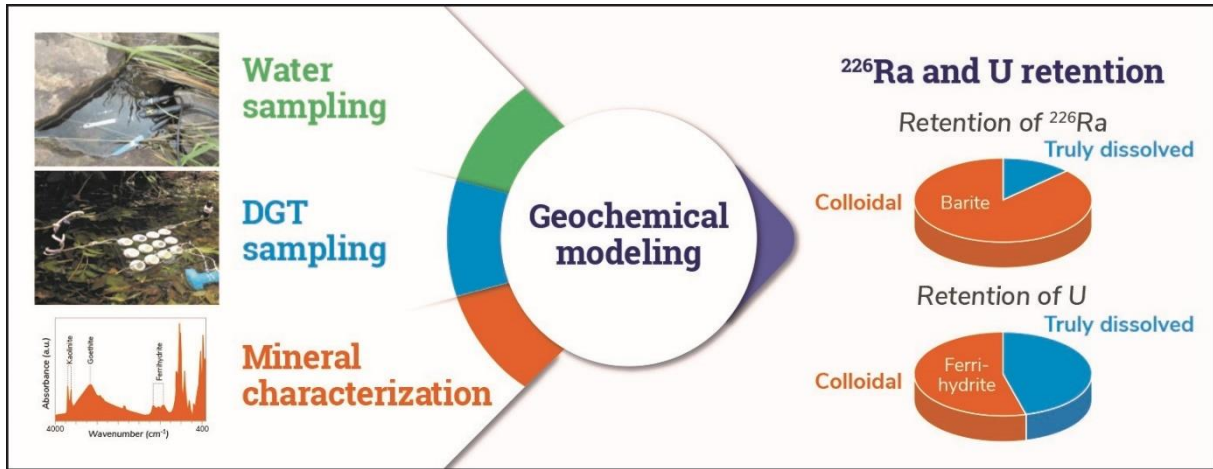
33

34 **Abstract**

35 The colloidal transport of trace (Fe, Al, Ba, Pb, Sr, U) and ultra-trace (^{226}Ra) elements was
36 studied in a mining environment. An original approach combining 0.45 μm filtered water
37 sampling, the Diffusive Gradient in Thin films (DGT) technique, mineralogical characterization,
38 and geochemical modelling was developed and tested at 17 sampling points. DGT was used
39 for the truly dissolved fraction of the elements of interest, while the 0.45 μm filtration includes
40 both colloidal and truly dissolved fractions (together referred to as total dissolved fraction).
41 Results indicated a colloidal fraction for Al (up to 50%), Ba (up to 86%), and Fe (up to 99%)
42 explained by the presence of submicrometric grains of kaolinite, barite, and ferrihydrite,
43 respectively. Furthermore, the total dissolved ^{226}Ra concentration in the water samples
44 reached up to 10-25 Bq/L ($1.2 - 3.0 \cdot 10^{-12}$ mol/L) at 3 sampling points, while the truly dissolved
45 aqueous ^{226}Ra concentrations were in the mBq/L range. Such high total dissolved
46 concentrations are explained by retention on colloidal barite, accounting for 95% of the total
47 dissolved ^{226}Ra concentration. The distribution of ^{226}Ra between the truly dissolved and
48 colloidal fractions was accurately reproduced using a $(\text{Ra}_x, \text{Ba}_{1-x})\text{SO}_4$ solid solution, with values
49 of the Guggenheim parameter a_0 close to ideality. ^{226}Ra sorption on ferrihydrite and kaolinite,
50 other minerals well known for their retention properties, could not explain the measured
51 colloidal fractions despite their predominance. This illustrates the key role of barite in such
52 environments. The measured concentrations of total dissolved U were very low at all the
53 sampling points ($<4.5 \cdot 10^{-10}$ mol/L) and the colloidal fraction of U accounted for less than 65%.
54 U sorption on ferrihydrite could account for the colloidal fraction. This original approach can be
55 applied to other trace and ultra-trace elements to complement when necessary classical
56 environmental surveys usually performed by filtration on 0.45 μm .

57 **Graphical abstract**

58



59

60 **Key words:** Colloidal transport, ²²⁶Ra, U, barite, ferrihydrite, DGT

61

62 1. Introduction

63 ^{226}Ra is one of the natural radionuclides resulting from the radioactive decay of ^{238}U . Due to its
64 long half-life (1600 y) and high specific activity (3.7×10^{10} Bq/g), ^{226}Ra is found at ultra-trace
65 level in the natural environment, usually below 1 Bq/L, *i.e.* 10^{-13} mol/L (Fesenko et al., 2014).
66 Because of its decay to ^{222}Rn , a radioactive gas with a short half-life (3.8 d) which can cause
67 health issues when inhaled depending on the concentration and the duration (WHO, 2009),
68 ^{226}Ra is subject to dedicated monitoring in environments of high uranium concentration such
69 as those of U mining (Landa, 2004; Liu et al., 2006), black shale mining (Phan et al., 2015;
70 Soesoo et al., 2020) and the production areas of phosphate fertilizers (Michie, 1979; IAEA,
71 2013). Monitoring the mobility of U and ^{226}Ra is important in these environments, especially
72 within the tailings storage facilities from U mining, which represent a worldwide volume of
73 around 1 billion m^3 (the last available worldwide inventory calculated in 2004 gives a total
74 volume of 908 million m^3) (IAEA, 2004). These tailings result from the extraction and processing
75 of U ore with a high yield, generally up to 96% (Déjeant et al., 2014). Despite this high yield,
76 tailings still contain about 85% of the radioactivity of the original ore, because the residual
77 radioactive products of ^{238}U such as ^{226}Ra (Yan and Luo, 2015) are concentrated within.
78 Tailings are generally stored under a rock cover or water layer to limit radon emission
79 (Robertson et al., 2018). Nevertheless, they are reactive systems (Martin et al., 2003; Patra et
80 al., 2011; Déjeant et al., 2016; Ballini et al., 2020; Seigneur et al., 2021; Lahrouch et al., 2022)
81 due to the potential mobilization of radionuclides enhanced by the fine crushing and chemical
82 treatment of the ore during the U-extraction process.

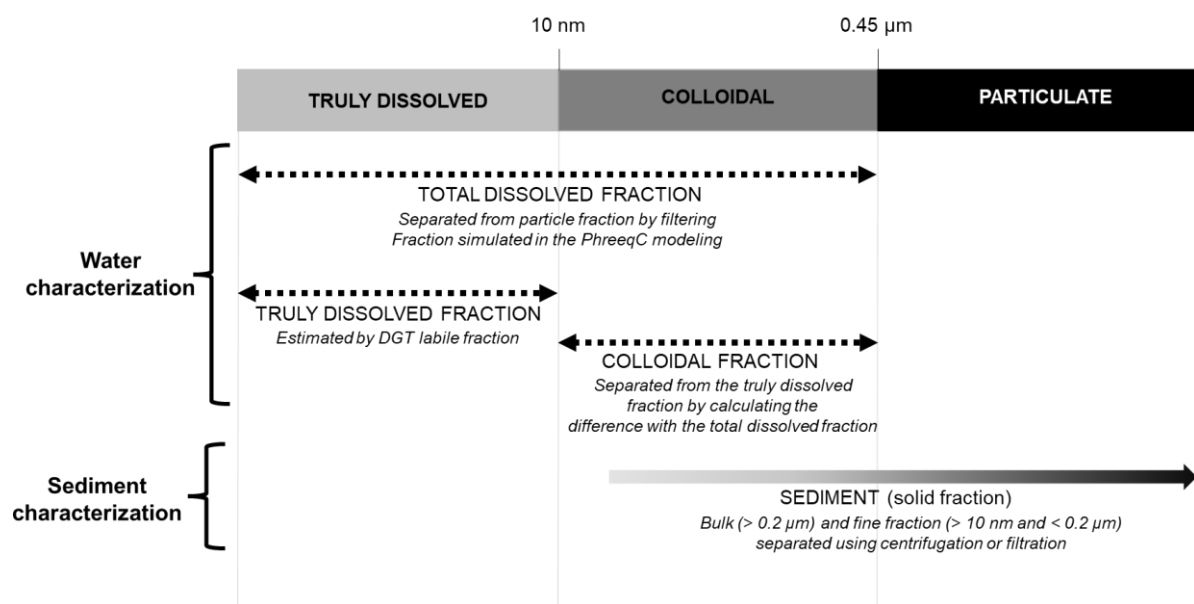
83 Uranium is particularly mobile under oxidizing conditions, where it occurs as the hexavalent
84 UO_2^{2+} uranyl species, and also in the presence of inorganic complexing agents such as sulfates
85 or carbonates which increase its aqueous mobility (Závodská et al., 2008; Langmuir and Riese,
86 1985). However, as a trace element, uranium mobility can be affected by sorption reactions on
87 the surface of minerals. In mining environments, U may be sorbed by clay minerals such as
88 montmorillonite or kaolinite (Sylwester et al., 2000; Schlegel and Descostes, 2009; Bachmaf
89 and Merkel, 2011; Tayal et al., 2019) or by iron oxyhydroxides such as ferrihydrite or goethite

90 (Ames et al., 1983; Missana et al., 2003; Leermakers et al., 2019; Lahrouch et al., 2021). ^{226}Ra
91 occurs mainly as free-ion Ra^{2+} in pH-neutral water of low salinity (Fesenko et al., 2014). It can
92 also form inorganic complexes with carbonate, chloride, and sulfate (Langmuir and Riese,
93 1985; Reiller and Descostes, 2020). Its mobility is also controlled by sorption reactions on the
94 surface of clay minerals (Reinoso-Maset and Ly, 2016; Robin et al., 2017) or manganese-iron
95 (oxy-)hydroxides (Ames et al., 1983; Nirdosh et al., 1990; Sajih et al., 2014). Furthermore,
96 radium can be incorporated into the structure of other alkaline earth sulfate or carbonate
97 minerals occurring in mining environments (Curie, 1911; Doerner and Hoskins, 1925; Langmuir
98 and Reise, 1985; Gnanapragasam and Lewis, 1995; Curti, 1999; Grandia et al., 2008; Yoshida
99 et al., 2008; McDevitt et al., 2019), such as barite, through the formation of a $(\text{Ba,Ra})\text{SO}_4$ solid
100 solution (Doerner and Hoskins, 1925; Brandt et al., 2015; Ouyang et al., 2019; Besançon et
101 al., 2020; Brandt et al., 2020). Sorption of U and ^{226}Ra on natural organic matter has also been
102 documented (see Bordelet et al. (2018) and references therein).

103 In natural waters, trace elements including radionuclides can be distributed into three fractions
104 distinguished by their difference in size (Figure 1): the particulate fraction greater than $0.45\ \mu\text{m}$
105 (corresponding to the water filtration threshold usually adopted for environmental monitoring),
106 the truly dissolved fraction lower than $1\ \text{nm}$ and the colloidal fraction with a size between these
107 two fractions (Stumm, 1997; Missana et al., 2004; Aiken et al., 2011). Colloids are mainly
108 composed of minerals exhibiting retention properties towards trace elements such as Fe-Ti-Al
109 oxy-hydroxides, phosphates, carbonates, sulfates, silica, and aluminosilicate phases found in
110 oxidizing contexts, and sulfides under reducing conditions (Kaplan et al., 1994; Turrero et al.,
111 1995; Porcelli et al., 2001; Nordstrom, 2011; Nordstrom et al., 2015; Husson et al., 2019; Javed
112 et al., 2020; Equeenuddin et al., 2020; Silva et al., 2021). They can also be a mix of organic
113 substances and minerals (Kretzschmar and Schäfer, 2005; Wang et al., 2013; Wang et al.,
114 2014; Novotnik et al., 2018). Due to their size and high specific surface areas (Buffle and
115 Leppard, 1995), they may be involved in the transport of trace elements as sorbed species in
116 the aquatic environment, including radionuclides.

117 The “total dissolved fraction” combines in this article the truly dissolved and colloidal fractions.
118 The particulate and total dissolved fractions can be easily determined by filtration (usually at
119 0.2 μm or 0.45 μm), but the colloidal fraction is rarely separated from the other fractions.
120 Nevertheless, some studies have evaluated the colloidal transport of U and other metals into
121 the environment by directly characterizing the colloidal fractions recovered after sampling to
122 show the important role of colloids in the transport. For example, colloidal fractions have been
123 extracted from both water and soil samples by asymmetric flow field-flow fractionation (As-FI-
124 FFF) and then characterized by coupling multi-angle laser light scattering (MALS), ultra-violet
125 (UV) and inductively coupling plasma-mass spectrometry (ICP-MS) techniques (Claveranne-
126 Lamolère et al., 2009; Harguindeguy et al., 2019). Several studies have tried with success to
127 evaluate the colloidal fractions of collected natural waters using both aqueous (membrane
128 filters, ultrafiltration, Diffusive Gradients in Thin Films - DGT) and solid characterizations (X-
129 ray diffraction - XRD; scanning electron microscopy with energy-dispersive X-ray spectroscopy
130 - SEM/EDX; transmission electron microscopy - TEM; time-resolved laser-induced
131 fluorescence spectroscopy - TRLIFS) (Backhus et al., 1993; Denaix et al., 2001; Wang et al.,
132 2013; Phrommavanh et al., 2013; Leermakers et al., 2016; Equeenuddin et al., 2020). These
133 methods are difficult to implement. Indeed, any change in the water composition, pH or
134 oxidation state during extraction operations may drastically change the colloidal distribution of
135 the trace elements. This is particularly the case for anoxic waters which samples may undergo
136 oxidation, with the consequent precipitation of ferric hydroxides and participation in the sorption
137 of ions, which would lead to an overestimation of the colloidal fraction. Surprisingly, the case
138 of ^{226}Ra is rarely addressed (Phrommavanh et al., 2013; Leermakers et al., 2016) and only a
139 few references present the role of barite in the colloidal transport of ^{226}Ra despite its well-
140 known retention properties.

141 In the present study, an innovative and complete multidisciplinary approach is proposed to
 142 assess the colloidal transport of uranium and ^{226}Ra . It includes water sampling by conventional
 143 filtration at $0.45\ \mu\text{m}$ and the DGT technique to estimate the truly dissolved fraction, from which
 144 the colloidal fraction could be calculated by difference. Although DGT and ultrafiltration are
 145 based on completely different principles, studies performed on the comparison of results
 146 obtained by the two methods show good agreement (Forsberg et al., 2006; Tonello et al., 2011;
 147 Leermakers et al., 2016). Sediments associated with these waters were also sampled and their
 148 mineralogy was characterized using XRD, infrared spectroscopy (IR), and SEM. All these data
 149 were completed by geochemical modelling to ensure consistency of the results and to better
 150 constrain the retention mechanisms of ^{226}Ra and U on the colloidal fraction. These data were
 151 acquired on a reclaimed former uranium mining site where a variety of geochemical conditions
 152 is encountered, including U and ^{226}Ra concentrations above the natural geochemical
 153 background.



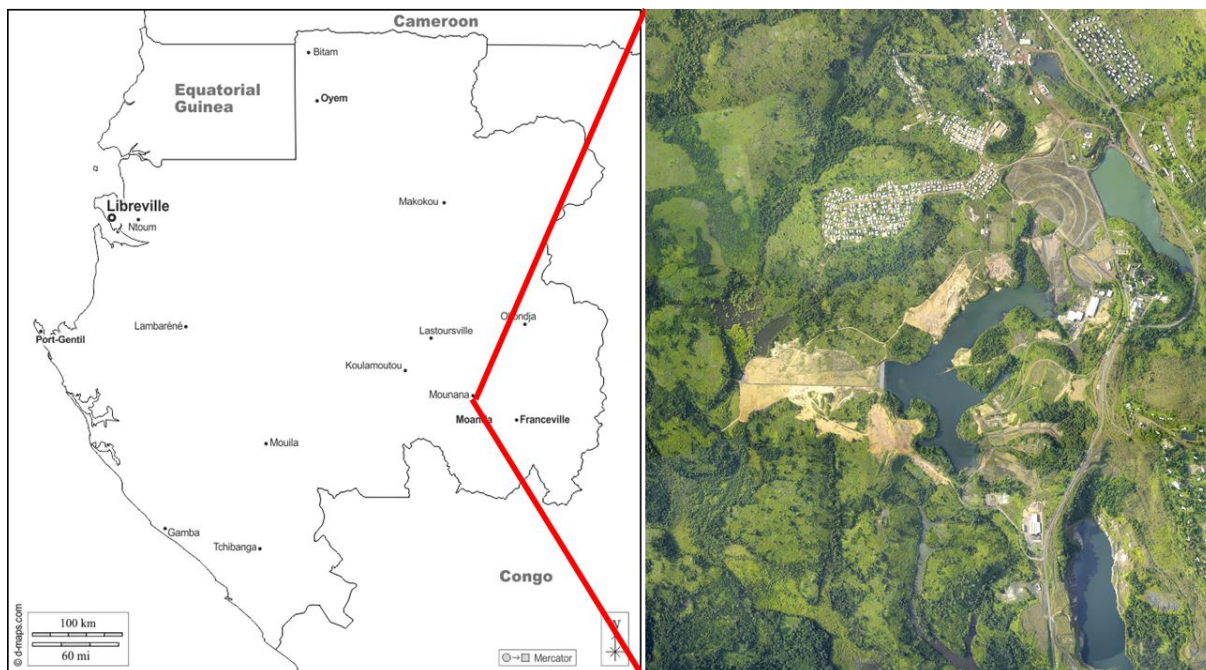
154

155 *Figure 1. Definition and characterization of the fractions sampled in surface waters.*

156

157 **2. Study area**

158 Mine water samples were collected at the former COMUF (Compagnie des Mines d'Uranium
159 de Franceville) uranium mining site in Gabon (Figure 2). From 1958 to 1999, COMUF mined
160 uranium deposits both in open pits and underground mines at the following locations around
161 the locality of Mounana: Mounana, Boyindzi, Oklo, Okélobondo and Mikouloungou (see
162 Lecomte et al., 2020 and references therein). In total, more than 6.4 Mt of ore with an average
163 grade of 3.73‰ was mined then processed in a plant located on-site to recover the uranium.
164 COMUF produced over 26,600 tons of uranium. Following the fall in uranium prices in the
165 1990s and the depleted mineral deposits, COMUF started rehabilitating the sites in 1997 and
166 ceased mining operations in June 1999 (Loueyit et al., 2002). Rehabilitation was completed in
167 2006 and included the five tailings storage facilities (Pagel and Somot, 2002). The sites are
168 now kept under radiological and environmental surveillance (water, soil, air, and food chain).
169 In this study, the focus was on 17 sampling points throughout the entire site characterized by
170 differences in the chemistry of the sampled water (see Table SI- 1 in Supplementary
171 Information), including leaching tailing waters. All water leaving the mining site has ^{226}Ra and
172 U concentrations at or below the natural background.



173

174 *Figure 2. Location of the COMUF mining site and aerial photo of the site in its present state.*

175

176 3. Materials & Methods

177 3.1. Water sampling and analysis

178 Mine water samples from 17 sampling points were taken and analyzed. The samples were
 179 extracted with a syringe through a pre-weighed 0.45 μm syringe filter (Durapore, Millipore)
 180 immediately after collection and conditioned just after the sampling. The filtration separated
 181 the particulate fraction ($>0.45 \mu\text{m}$) from the total dissolved fraction ($<0.45 \mu\text{m}$). The physico-
 182 chemical parameters (pH, oxidation reduction potential – ORP, dissolved O_2 , electrical
 183 conductivity - EC, and T°) were measured *in-situ* at each of the seventeen sampling points.
 184 The values were recorded once the stabilization of the physico-chemical parameters had been
 185 reached. For more details regarding the sampling and analytical methodologies, refer to
 186 (Phrommavanh et al., 2013; Wang et al., 2014; Ballini et al., 2020).

187 The total dissolved fraction was analysed for:

- 188 - Major cations (Ca, Mg, K, Na) by inductively coupled plasma atomic emission
 189 spectrometry (ICP-AES; Iris, Thermo Jarrell Ash). Yttrium and gold (1 ppm) were used

190 as internal standards and reference materials SW1 (surface water level 1), and SW2
191 (surface water level 2) were used as quality control (QC).

192 - Major anions (Br, F, Cl, SO₄) by ion chromatography (Dionex DX 500). Ammonium,
193 nitrate, phosphate, and silicate were determined colorimetrically (QuAAtro Seal
194 Analytical). The reference material ION-96 (NRCC) was used as QC. Dissolved
195 inorganic carbon (DIC) was obtained by mass spectrometry (Nu Instruments Ltd.).
196 Sodium bicarbonate was used as a standard and ION-96 (NRCC) as a QC sample.

197 - Trace element concentrations (Al, Ba, Fe, Pb, Sr, U, ²²⁶Ra) using a Thermo Element II
198 sector field inductively coupled plasma mass spectrometry (SF-ICP-MS), based upon
199 calibration curves prepared from multi-element (Merck) and single element (Johnson
200 Matthey Specpure) standard solutions. SLRS-4 (river water) and NIST-1640a reference
201 samples were used as QC samples.

202 All measurements were within the certified ranges, with recoveries ranging from 95-105%.

203

204 3.2. DGT measurements

205 The DGT technique (Davison and Zhang, 1994; Phrommavanh et al., 2013; Drozdak et al.,
206 2015; Drozdak et al., 2016; Leermakers et al., 2016; Husson et al., 2019) was used to
207 estimate the truly dissolved fraction. This technique, developed by Davison and Zhang (1994)
208 consists of trapping the elements of interest on a passive sampler comprising a binding gel, a
209 diffusion gel, and a filter membrane. Species small enough to diffuse into the diffusive gel
210 (generally around 10 nm pore size) and kinetically sufficiently labile to dissociate within the
211 residence time in the diffusive layer (free metal ions and labile metal complexes) will be trapped
212 on the binding gel.

213 Polyacrylamide (PAM) diffusive gels with a thickness of 0.8 mm were prepared according to
214 Zhang and Davison (2000). They contained 15% of acrylamide solution and 0.3% of patented
215 agarose derived cross-linker (DGT Research Ltd. Lancaster). The catalyst used was

216 N,N,N',N'-tetramethylenediamine (TEMED) and 10% ammonium persulfate was used as an
 217 initiator for polymerization. The diffusive gels were stored in a 0.01 M NaNO₃ solution before
 218 use. PAM binding gels of 0.4 mm of thickness were prepared with either 1 g of MnO₂ dedicated
 219 to ²²⁶Ra (prepared according to Leermakers et al., 2016) or 2 g of Chelex-100 resin dedicated
 220 to other trace elements (prepared according to Zhang and Davison, 2000). The Chelex and
 221 MnO₂ binding gels were eluted in 1 mL of 1 M HNO₃ solution for 24 hours. Samples were then
 222 further diluted to 10 mL and the resin gel was removed before ICP-MS analysis. The mass (m)
 223 of metal accumulated on the resin gels was calculated using equation (1), considering the
 224 concentration measured by ICP-MS (C_e), the volume of gel (V_g), the total elution volume (V_e)
 225 and the elution factor (f_e) (Leermakers et al., 2009; Drozdak et al., 2015).

$$226 \quad m = \frac{C_e(V_g + V_e)}{f_e} \quad (1)$$

227 The DGT-measured labile concentration (C_{DGT}) (g cm⁻³) was then deduced using the equation
 228 (2), considering the mass of the analyte on the binding gel (m) (expressed in grams), the
 229 thickness of the diffusive gel and filter (Δg) (in cm), the diffusion coefficient of the analyte in
 230 the diffusive gel (D) (in cm² s⁻¹), the deployment time (t) (in s) and the surface area of the
 231 exposure window (A) (in cm²).

$$232 \quad C_{DGT} = \frac{m \cdot \Delta g}{D \cdot t \cdot A} \quad (2)$$

233 The diffusion coefficients used are from Davison (2016) and Drozdak et al. (2016) for uranium
 234 and from Leermakers et al. (2009) for ²²⁶Ra. They were corrected for temperature using the
 235 Stokes-Einstein equation (Zhang and Davison, 1999). DGT-labile Al, Ba, Fe, Pb, Sr, U and
 236 ²²⁶Ra concentrations were measured for ten of the seventeen sampling points using this
 237 technique and used to estimate the truly dissolved fraction. DGT deployment times ranged
 238 from 24h to 72h depending on the expected concentrations.

239

240 3.3. Colloidal fraction

241 The colloidal concentrations of the targeted elements were determined by calculating the
242 difference between the total dissolved (<0.45 μm) and DGT-measured truly dissolved fractions
243 according to Equation (3):

$$244 \quad [\text{Element}]_{\text{colloidal}} = [\text{Element}]_{\text{total dissolved (<0.45}\mu\text{m)}} - [\text{Element}]_{\text{truly dissolved (DGT)}} \quad (3)$$

245 They were calculated for the elements for which the DGT-labile fraction was measured.

246

247 3.4. Mineralogical characterizations

248 A mineralogical characterization based on the combination of XRD, Mid-InfraRed Fourier
249 Transform Infra-Red (MIR-FTIR), and Near-Infrared (NIR) spectroscopy and SEM/EDX was
250 carried out on the sediments collected in sample vials at the two sampling points where the
251 highest ²²⁶Ra colloidal fractions were measured (S8 and S11). This multimethodological
252 approach enables the occurrence of the mineral phases potentially involved in the retention of
253 colloidal U and ²²⁶Ra to be verified. The characterizations were conducted on two fractions for
254 both samples: the bulk fraction, to determine the global mineralogical composition; and the fine
255 fraction (below 2 μm), to characterize the finely divided minerals including clay minerals.

256 The fine fraction (supernatant fraction here) was extracted from the bulk fraction dispersed in
257 water using an ultrasonic bath and then centrifuged (2.5 minutes at 1000 rpm).

258 The mineral phases were determined using a Bruker D8 diffractometer (IC2MP, Poitiers)
259 equipped with a copper anode tube (Cu-Kα = 1.5418 Å). Data were acquired under the
260 following analytical conditions: 40 kV, 40 mA, angular domain from 2 to 65 °2θ for the randomly
261 oriented powder of the bulk fraction, with a step of 1.2 s per 0.025 °2θ and from 2 to 35 °2θ for
262 oriented preparations of the fine fractions (air-dried and after ethylene glycol saturation in vapor
263 state).

264 Mid-infrared spectra (400 to 4000 cm⁻¹) were acquired on the bulk solid fraction using a
265 Nicolet™ 6700 spectrometer equipped with a potassium bromide (KBr) beamsplitter and a

266 DTGS-KBr detector. The obtained spectra are a coaddition of 100 scans with a resolution of
267 4 cm^{-1} . Ferrihydrite synthetization following the protocol from Cornell and Schwertmann (2003)
268 was used as a standard. Analyses of the bulk fraction were carried out on a blend of 1 mg of
269 sample and 150 mg of KBr which were then homogenized in a mortar and compressed at
270 8 kbar to form pellets. These were dried in an oven at $105\text{ }^{\circ}\text{C}$ for 24 h. The fine fraction was
271 analyzed using a Nicolet™ IS50 ATR equipped with a KBr beamsplitter and a DTGS-KBr
272 detector.

273 Near-infrared analysis of the bulk and fine fractions was used to determine the relative
274 proportions of kaolinite and smectite. Measurements were made with a Nicolet™ 6700
275 spectrometer equipped with a Thermo Scientific Near-Infrared integrating sphere, a PbSe
276 detector, and a CaF_2 beamsplitter. The obtained spectra (4000 to 10000 cm^{-1}) are a coaddition
277 of 100 scans with a resolution of 4 cm^{-1} . The data were converted from reflectance to
278 transmittance using OMNIC Series software in order to analyse the region from 4750 to
279 4000 cm^{-1} . The latter is used to define the relative proportion between kaolinite and smectite
280 according to the method developed by Hebert (2018).

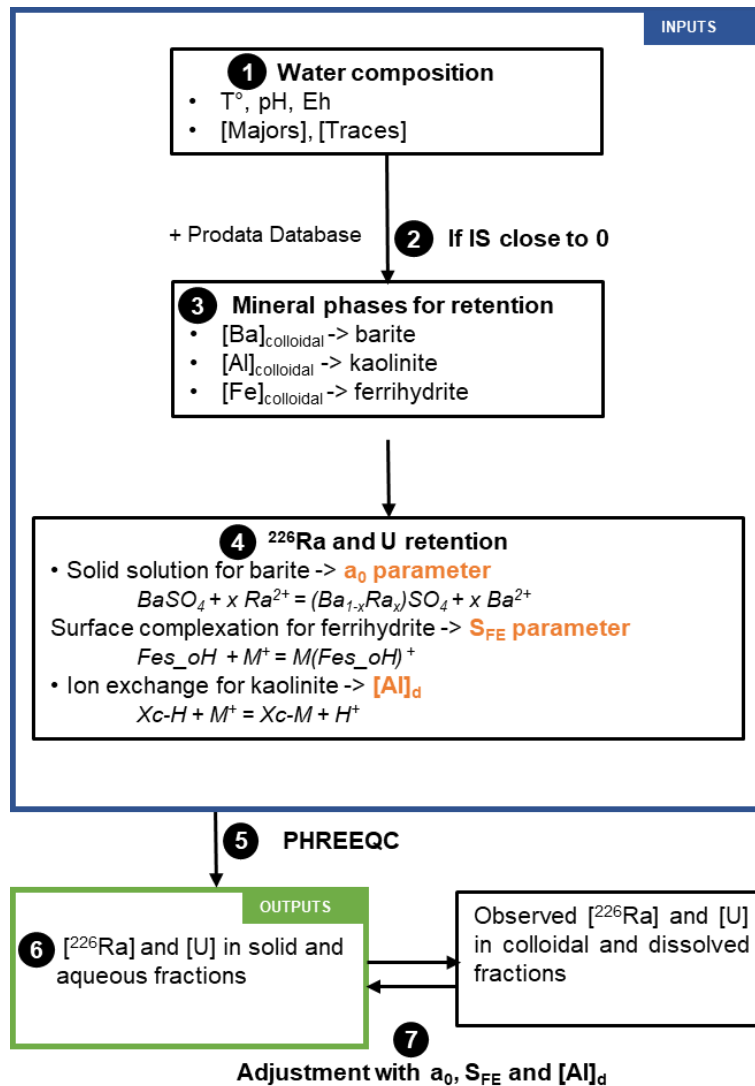
281 Then, SEM analysis was performed using a JEOL 5600 LV microscope coupled with a
282 BRUKER SiLi EDS AXS detector. The bulk solid fractions were crushed in a mortar and
283 compressed using a hand-held pelletizer to form pellets. These were coated with carbon to
284 perform chemical analyses (Si, Al, K, Fe, Ba, S) and observations. SEM observations were
285 made in backscattering electron mode (BSE) using the following analytical conditions: a
286 working distance of 16.5 mm, a probe current of 1 nA, and an acceleration voltage of 15 kV.

287

288 3.5. Geochemical modelling

289 Modelling was performed to test and confirm the colloidal transport of ^{226}Ra and U and to
290 quantify the contribution of each mineral phase involved in their retention. The PHREEQC
291 computer program (Parkhurst and Appelo, 2013; version 3.6.2) was used, implementing the

292 PRODATA thermodynamic database which focuses on U and ^{226}Ra chemistry (Reiller and
293 Descostes, 2020; version 1.1.0.4). The modelling approach is described in Figure 3.
294 Mineralogical observations and mineral species saturation indexes, calculated using the total
295 dissolved fractions implemented in the model, were used to ascertain the presence of minerals
296 involved in the retention of ^{226}Ra and U: clay minerals, iron oxy-hydroxides, and barite. The
297 main mechanisms considered were mineral precipitation and dissolution, sorption of cations
298 on ferrihydrite and kaolinite, and formation of the barite-based $(\text{Ba,Ra})\text{SO}_4$ solid solution. A
299 similar approach for Ra modelling using PHREEQC can be found in Van Sice et al. (2018) and
300 McDevitt et al. (2019).



301

302 *Figure 3. Modelling strategy for the partition of measured elements between colloidal and truly dissolved fractions*
 303 *in the water samples. T: temperature, IS: saturation index for minerals, a₀: parameter of deviation from an ideal*
 304 *solid solution, S_{FE}: specific surface area of ferrihydrite, [Al]_d: aluminum concentration measured in truly dissolved*
 305 *fraction, M: cation, Xc-: sorption site on clay minerals, Fes_: sorption site on iron oxy-hydroxide. The Prodata*
 306 *thermodynamic database includes the speciation of elements and the mineral phases with associated constants of*
 307 *dissolution/precipitation.*

308

309 The (Ba,Ra)SO₄ solid solution model was implemented using the dimensionless Guggenheim
 310 interaction parameter a₀ which represents the deviation from an ideal solid solution (Vinograd
 311 et al., 2013). ²²⁶Ra / U sorption onto ferrihydrite was implemented using the surface
 312 complexation model and site densities from Dzombak and Morel (1990). The surface

313 complexation constants are from Dzombak and Morel (1990) for H, Ca, Mg, Ba, SO₄, and U
314 with additions for carbonates from the Minteq database (minteq.v4.dat derived from Allison
315 and Brown, 1995) and for uranyl-carbonate from Mahoney et al. (2009). Surface complexation
316 constants for ²²⁶Ra and ferrihydrite surface areas are from Sajih et al. (2014). ²²⁶Ra / U sorption
317 onto kaolinite was implemented using the multi-site exchange ion model from Reinoso-Maset
318 and Ly (2016) with site concentrations, major cations, and ²²⁶Ra and U sorption constants from
319 Reinoso-Maset and Ly (2014, 2016). Ba sorption was implemented with the same constants
320 as ²²⁶Ra sorption as they are chemical analogues (Curie, 1911; Sajih et al., 2014).

321 As inputs to the model, the colloidal fractions of Ba, Fe, and Al measured with equation (3),
322 when positive, were implemented as quantities of barite, ferrihydrite, and kaolinite respectively.
323 The initial water chemistry was implemented in the model using major and trace element
324 concentrations and physico-chemical parameters measured *in-situ* as described in section 3.a.
325 Therefore, the total amounts of ²²⁶Ra and U were inserted into the model and were redistributed
326 between the aqueous fraction (i.e. the truly dissolved) and the solid fraction (representative of
327 the colloidal fraction) through the equilibrium calculations.

328

329 **4. Results**

330 4.1. Water chemistry

331 All results are given in Table SI- 1. The surface water samples are slightly acidic to neutral ,
332 with pH values ranging from 4.8 to 7.5. Furthermore, they are very weakly mineralized with
333 electrical conductivities below 200 μS/cm, and consequently show very low major ion
334 concentrations (ionic strength in the range of 10⁻³ mol/L). The total dissolved carbon
335 concentrations are also very low (<1 mmol C/L), with carbon mainly inorganic. In general the
336 samples exhibit a calcium bicarbonate type, with a few presenting slightly higher
337 concentrations of sodium and sulfate (see Figure SI- 1). Most of them are oxygenated with
338 oxidizing ORP values from 174 to 592 mV/SHE. The analyses displayed a relatively
339 satisfactory ionic balance allowing these results to be used, even if ionic deviations are

340 observed for very diluted samples. The water samples can be divided into two categories
341 according to their chemistry and their ^{226}Ra content. In one, we can group the weakly
342 mineralized (conductivity $<75 \mu\text{S}/\text{cm}$) and slightly acidic samples (S1, S3, S4, S5, S6, S7, S12,
343 S13, S14, S16, and S17). In all these, the water, being very pure and comparable to rainwater,
344 is chemically aggressive towards rocks and soils from the watershed and exhibits the highest
345 Al concentrations. In the other category, slightly more mineralized water (conductivity >150
346 $\mu\text{S}/\text{cm}$) can be identified (S2, S8, S9, S11, S15, and to a lesser extent S10). The water at these
347 points has been affected by the former U mining activities. In this group, the highest total
348 dissolved concentrations of ^{226}Ra ($>10 \text{ Bq}/\text{L}$ for S8, S11, and S15) and to a lesser extent U
349 ($\geq 40 \text{ nmol}/\text{L}$ for S2 and S9) can be observed concurrently with enrichments in Na, Ca, Mg,
350 SO_4 , NO_3 , DIC, and also in trace elements such as Ba, Fe, and Sr, which are linked to the
351 phases involved in the ^{226}Ra and U retention (sulfate minerals and ferric oxy-hydroxides). This
352 is also highlighted by the correlation matrix gathered in Table SI- 2 ($R^2_{[^{226}\text{Ra}]-\text{EC}} = 0.67$; $R^2_{[^{226}\text{Ra}]-$
353 $[\text{Na}]} = 0.59$; $R^2_{[^{226}\text{Ra}]-\text{DIC}} = 0.90$; $R^2_{[^{226}\text{Ra}]-[\text{NO}_3]} = 0.84$; $R^2_{[^{226}\text{Ra}]-[\text{NH}_4]} = 0.97$; $R^2_{[^{226}\text{Ra}]-[\text{Sr}]} = 0.68$;
354 $R^2_{[^{226}\text{Ra}]-[\text{Ba}]} = 1.00$; $R^2_{[^{226}\text{Ra}]-[\text{Fe}]} = 0.94$). No clear correlation involving U is discernible. High
355 concentrations in ^{226}Ra above $10 \text{ Bq}/\text{L}$ are anomalous and will be discussed below.

356 It is interesting to note that the calculated activity ratio $^{238}\text{U}/^{226}\text{Ra}$ for each sample point is far
357 from being equal to 1, as would be expected if radioactive equilibrium had been reached; but
358 was in general less than 1, which is consistent with U-depleted tailings. However, ratios greater
359 than 1 are also observed at 2 points, S2 (5.6) and S10 (9.5), indicating an excess of U. This U
360 excess, indicating the presence of ^{238}U not at secular equilibrium, is due to a redistribution of
361 U after ore processing. These observations agree with the different geochemical properties of
362 both the radioelements relative to redox conditions and the retention minerals leading to
363 differences in their respective mobility, especially when they are at ultra-trace levels.

364

365 4.2. Truly dissolved fraction measured by DGT and colloidal fraction

366 DGT-labile Al, Ba, Fe, Pb, Sr, U, and ²²⁶Ra concentrations were measured for ten of the
367 seventeen sampling points (see Table SI- 3 in Supplementary Information). DGT-labile Al, Ba,
368 Sr, and Pb show concentrations and variations in the same range as those observed for total
369 dissolved concentrations: ([Al]_{DGT} from 16 (S7) to 450 (S4) nmol/L; [Ba]_{DGT} from 38 nmol/L (S7)
370 to 2.395 μmol/L (S15); [Pb]_{DGT} from 10.7 (S2) to 197 (S17) pmol/L; [Sr]_{DGT} from 25.9 (S7) to
371 213 (S9) nmol/L). However, lower concentrations of truly dissolved ²²⁶Ra are found with
372 activities varying between 0.99 (S1) and 1395 (S11) mBq/L, accounting for 4-96% of the total
373 dissolved ²²⁶Ra, whereas the truly dissolved uranium concentrations range between 0.04 (E1)
374 and 37.3 (S2) nmol/L and account for 40-98% of the total dissolved uranium. For Fe, on the
375 other hand, the DGT-labile concentrations ([Fe]_{DGT} from 1.85 nmol/L (S2) to 10.8 μmol/L (S11))
376 account for <1% to 42% of the total dissolved Fe concentrations.

377

378 Low DGT-labile concentrations are also observed to a lesser extent for the highest
379 concentrations of ²²⁶Ra and Ba. Such differences are associated with the existence of a
380 colloidal fraction as calculated using Eq. (3) (results are presented in Table 1). From the
381 samples where colloidal fraction was measured, the majority of Fe is transported as colloids
382 (90% on average) as well as alkaline earths Ba, Sr, and ²²⁶Ra, which show high colloidal
383 transport (respectively 73%, 78 and 71% on average) even in low-mineralized waters. A lower
384 proportion of U (40%) is transported as colloids. The highest ²²⁶Ra colloidal concentrations
385 (9 868 mBq/L; S11: 26 405 mBq/L (S11); 24 725 mBq/L (S15)) are observed jointly with the
386 highest colloidal concentrations of Fe (8.01 μmol/L (S8); 49.95 μmol/L (S11); 48.66 μmol/L
387 (S15)) and Ba (3 481 nmol/L (S8); 10 058 nmol/L (S11); 8 788 nmol/L (S15)). This is also
388 confirmed by the correlation matrix presented in Table SI- 2 ($R^2_{[226\text{Ra}]_{\text{coll}}-[Fe]_{\text{coll}}} = 0.98$; $R^2_{[226\text{Ra}]_{\text{coll}}-[Ba]_{\text{coll}}} = 1.00$). No correlation involving U is found ($R^2_{[U]_{\text{coll}}-[Fe]_{\text{coll}}} = -0.43$). These results highlight
390 the possible retention of ²²⁶Ra, by Ba and/or Fe-bearing minerals. Note that negative colloidal
391 concentrations are typically found for very low total dissolved concentrations, and are assigned
392 to 0 in the balance of this study. As regards the trace and ultra-trace elements, they result from

393 both the uncertainties for very low concentrations and the slight variations in water composition
 394 during the DGT deployment time (see Figure SI- 2).

395 *Table 1. Colloidal concentrations and molar fractions of Al, Ba, Fe, Pb, Sr, U, and ²²⁶Ra measured for 10 sampling*
 396 *points (see Eq. 3 for calculation). N/A is reported when the calculation was not possible, e.g. when total dissolved*
 397 *concentrations are below the detection limit as for ²²⁶Ra. Shown in grey are the samples for which a mineralogical*
 398 *characterization of the suspended matter was achieved.*

	[Al] _{colloidal}	[Ba] _{colloidal}	[Fe] _{colloidal}	[Pb] _{colloidal}	[Sr] _{colloidal}	[²²⁶ Ra] _{colloidal}	[U] _{colloidal}
	(nmol/L)	(nmol/L)	(μ mol/L)	(pmol/L)	(nmol/L)	(mBq/L)	(nmol/L)
S1	135 26%	N/A	3.05 79%	7.37 10%	N/A	N/A	0.06 56%
S2	11 13%	163 75%	0.395 100%	66.57 86%	622 79%	4.16 17%	8.78 19%
S3	60 16%	N/A	0.631 58%	N/A	N/A	46.13 57%	1.36 50%
S4	N/A	N/A	1.86 96%	235 89%	N/A	213.3 82%	2.69 65%
S7	60 79%	63 62%	0.938 99%	18.67 52%	63.77 71%	N/A	0.12 59%
S8	N/A	3481 76%	8.01 95%	9.19 21%	544 79%	9868 96%	2.44 47%
S9	N/A %	325 60%	1.74 94%	N/A	537 72%	299 69%	8.21 18%
S11	94 47%	10058 86%	49.95 82%	N/A	792 88%	26405 95%	0.17 7%
S15	756 97%	8788 79%	48.66 98%	1176 87%	677 78%	24725 96%	N/A
S17	89 57%	N/A	4.33 91%	202 51%	N/A	109.2 57%	2.54 51%

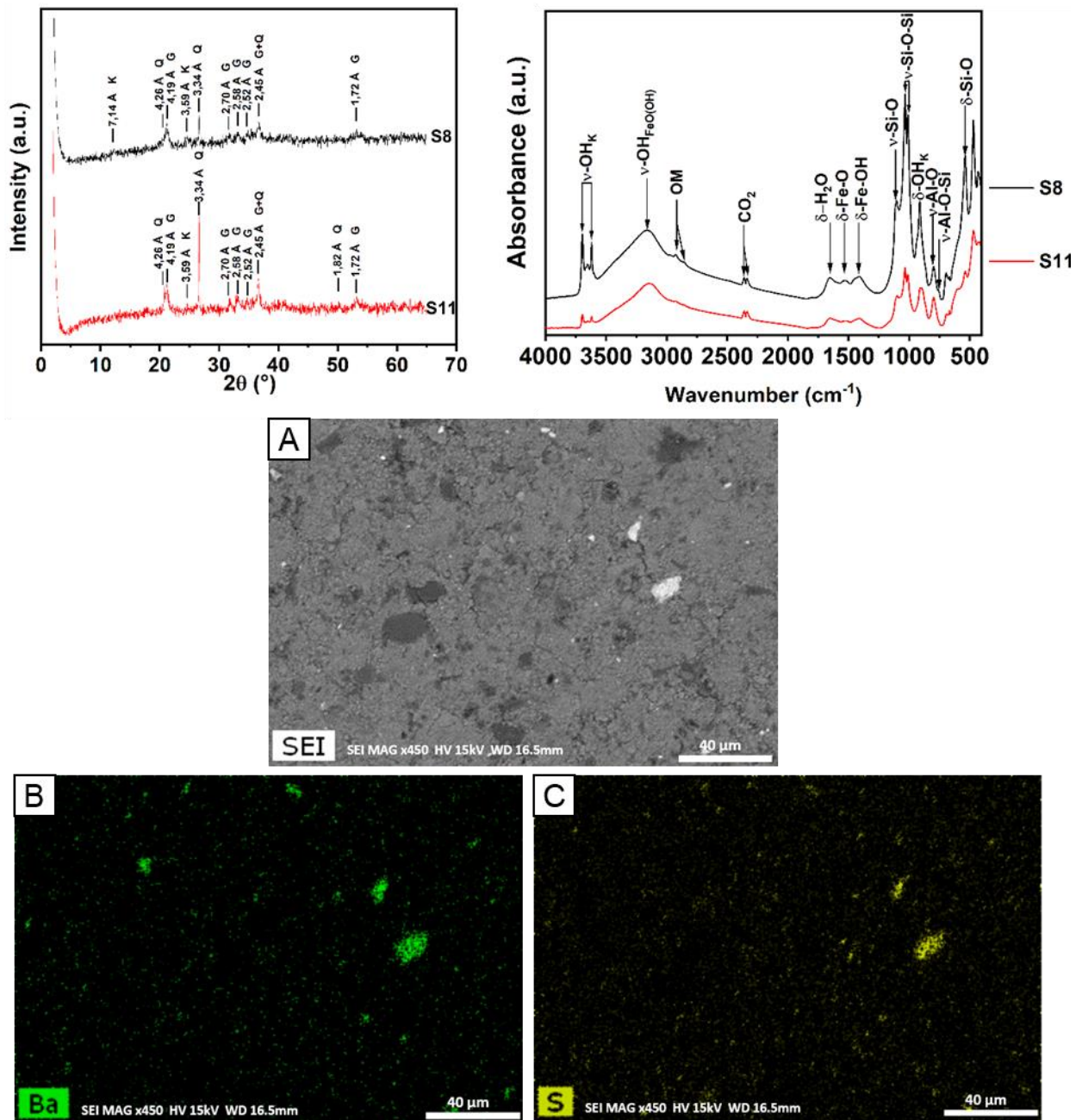
399

400

401 4.3. Mineralogical characterization

402 Sediments collected from two sampling points where the highest ²²⁶Ra colloidal fraction was
 403 measured (S8 and S11) were characterized. The XRD patterns obtained on the bulk fraction
 404 of the suspended solids (Figure 4) show occurrences of quartz, goethite, and kaolinite (only
 405 for S8). The fine fraction was used to determine the presence of clay particles (Figure SI- 3).
 406 XRD measurements of the latter confirmed that both samples contained kaolinite and goethite.
 407 The XRD analysis also indicated the presence of illite or micas (peak at 9.99 Å) in one sample.

408 Additional SEM-EDX analyses confirmed it is mica. Furthermore, the bulk fraction XRD
 409 patterns exhibit a low signal-to-noise ratio, which can be attributed to amorphous phase(s).



410
 411 *Figure 4. Mineralogical characterization of the samples S8 and S11 by: TOP: XRD (left: XRD patterns of the bulk*
 412 *fraction. For better legibility, the S11 curve has been offset. Abbreviations: K: Kaolinite. Q: Quartz. G: Goethite) and*
 413 *Mid-infrared spectroscopy (right; spectra of the bulk fraction. For better legibility, the S8 curve has been offset);*
 414 *BOTTOM: SEM observations of barite (A) combined with EDX maps for barium (B) and sulfur (C) on bulk solid*
 415 *fraction.*

416

417 Infrared analyses confirmed the presence of kaolinite and goethite in both fractions for both
418 samples (see Figure 4 and Figures SI- 4, SI- 5, SI- 6 and SI- 7 in Supplementary Information).
419 Infrared analyses of the fine fractions showed the presence of kaolinite and to a lesser extent
420 smectite with a ~90/10 kaolinite/smectite ratio. SEM observations revealed the presence of
421 barite in the bulk fraction for both samples, from micrometric to submicrometric dimensions
422 (Figure 4).

423

424 **5. Discussion: highlighting the ²²⁶Ra and U retention properties of the colloidal fraction** 425 **by modelling**

426 The mineralogical characterizations have highlighted barite, kaolinite, and iron oxyhydroxides
427 as minerals present in the samples and known for their properties to incorporate ²²⁶Ra and U.
428 The goethite observed in the samples might originate from ferrihydrite after oven drying, the
429 observed red color of the samples during sampling indicates the presence of ferrihydrite. The
430 stability of these minerals was confirmed by calculating the saturation indexes for each of them:
431 barite (the extreme values range from -2.52 to 1.18 for samples S1 and S11, respectively),
432 ferrihydrite (from 0.40 to 1.89 for samples S13 and S11, respectively) and kaolinite (from -1.11
433 to 4.93 for samples S1 and S6, respectively) for total dissolved fraction and for truly dissolved
434 fraction (extreme values are -2.49 to 0.5 for barite, -2.78 to 1.12 for ferrihydrite and -1.3 to 4.9
435 for kaolinite in this case). Carbonates, hydroxide, and sulfate minerals other than barite (calcite,
436 cerussite, rhodochrosite, anglesite, celestite, gypsum) but also U-bearing minerals
437 (metaschoepite and soddyite) are undersaturated (SI <-1).

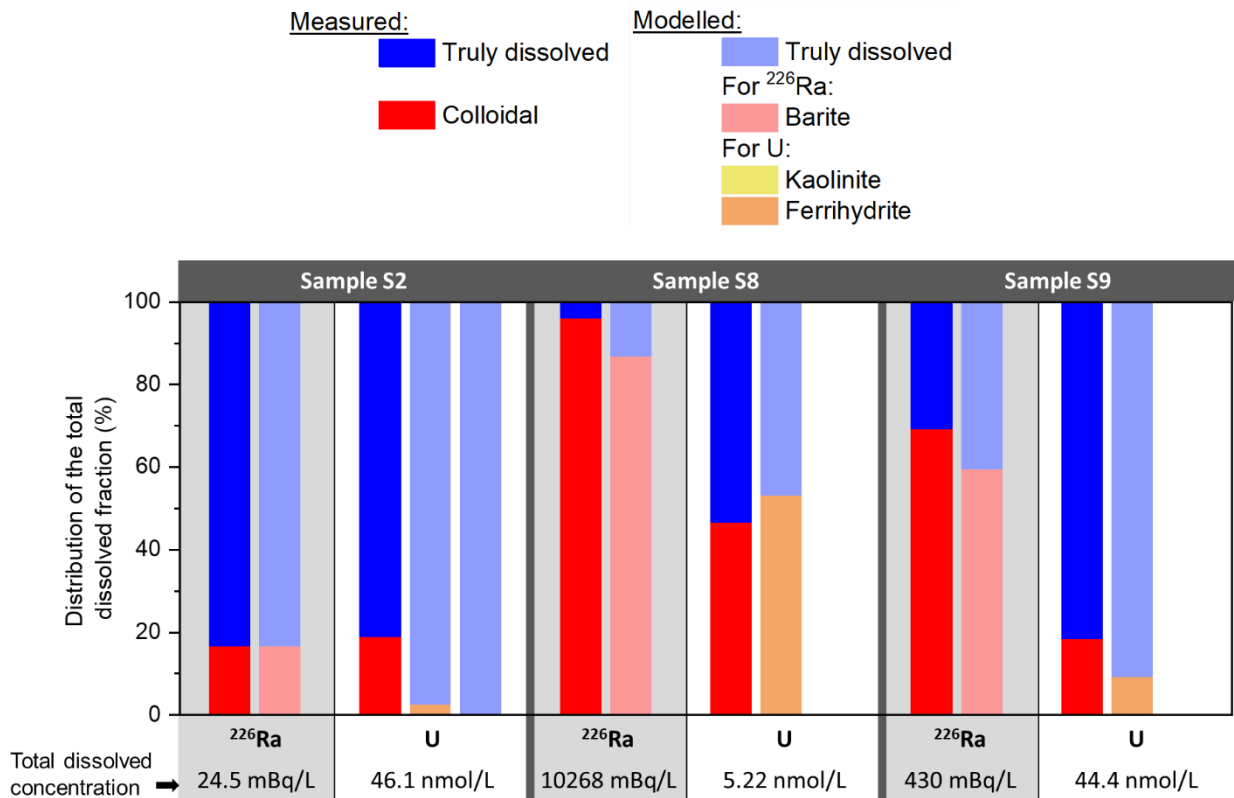
438

439

5.1. ^{226}Ra retention on barite

440 Modelling of ^{226}Ra retention by solid solution or sorption was performed as described in Figure
441 1 for the sampling points where colloidal ^{226}Ra was measured as well as colloidal Ba (5
442 samples: S2, S8, S9, S11, S15), Fe (8 samples: S2, S3, S4, S8, S9, S11, S15, S17) or Al (5
443 samples: S2, S3, S11, S15, S17). The ^{226}Ra measured in the total dissolved fraction was set
444 as an/the input to the model and was redistributed between the modelled truly dissolved and
445 colloidal fractions, either barite, kaolinite or ferrihydrite (only elements for which colloidal
446 fractions were measured were considered as potentially forming a solid phase, therefore
447 excluding Mn). Ferrihydrite was chosen as the most challenging case as it is the iron
448 oxyhydroxide with the greater sorption capacity.

449 The incorporation of ^{226}Ra in the barite solid solution as $(\text{Ra}_x, \text{Ba}_{1-x})\text{SO}_4$ was modelled by
450 adjusting the Guggenheim parameter a_0 (Guggenheim, 1937; Glynn, 2000) to approximate the
451 measured distribution of ^{226}Ra . The dimensionless Guggenheim interaction parameter a_0
452 represents the deviation from an ideal solid solution (Vinograd et al., 2013). As shown in Figure
453 5, the distribution of ^{226}Ra between the truly dissolved and colloidal fractions was accurately
454 reproduced simply by using a $(\text{Ra}_x, \text{Ba}_{1-x})\text{SO}_4$ solid solution with a_0 values close to ideality. A
455 solid solution is considered as ideal when $a_0 = 0 \pm 0.3$ (Heberling et al., 2018) and non-ideal
456 for a_0 values below 2.5 (Curti et al., 2010). The calculated a_0 value for samples S2 therefore
457 slightly diverges from the ideal solid solution (Table 2). These two points have the lowest
458 $[\text{}^{226}\text{Ra}]_{\text{colloidal}}$ (4.16 and 299 mBq/L representing respectively 17% and 69% of the total
459 dissolved ^{226}Ra) and $[\text{Ba}]_{\text{colloidal}}$ (163 and 325 nmol/L, 75% and 60% of Ba) calculated values,
460 which could lead to greater measurement uncertainties (see Table 1).



461

462

Figure 5: Modelling of the ^{226}Ra and U retention on the colloidal fraction. The truly dissolved fraction ^{226}Ra and U

463

retention on colloidal fraction were tested independently on ferrihydrite and kaolinite but retention was negligible

464

for ^{226}Ra . Barite was also tested for ^{226}Ra retention. Three representative samples are represented here, the other

465

samples can be found in Supplementary Information (Figure SI-8).

466

467

A solid solution close to ideality accounts for the great majority of colloidal ^{226}Ra . The

468

distribution of ^{226}Ra between barite and solution can be also described by a partition coefficient,

469

D:

470

$$D = \frac{\left(\frac{Ra}{Ba}\right)_{barite}}{\left(\frac{Ra}{Ba}\right)_{solution}} = \frac{\left(\frac{[^{226}Ra]_{colloidal}}{[Ba]_{colloidal}}\right)}{\left(\frac{[^{226}Ra]_{DGT}}{[Ba]_{DGT}}\right)} \quad (4)$$

471

The partition coefficients for the measured and modeled solutions are listed in Table 2.

472 Table 2. a_0 and partition coefficient (D) values corresponding to the modelled and measured values of Ra and Ba
 473 for a $(Ra_xBa_{1-x})SO_4$ solid solution. A tolerance of 10% was considered for the truly dissolved and total dissolved
 474 concentrations.

Sampling point	a_0 modeled	D modeled	D measured
S2	0.8	0.8	0.07±0.04
S8	0	1.7	8±5
S9	0	1.7	1.5±0.9
S11	0.3	1.4	3±2
S15	0	1.8	7±4

475
 476 The partition coefficients calculated using the measured concentrations (D measured) are for
 477 three samples higher than those modelled, reaching values up to 8±5 which is higher than the
 478 usual partition coefficients for the $(Ra_x, Ba_{1-x})SO_4$ solid solution system, with values ranging
 479 from 0.1 to 2.1 (Curti et al., 2010; Heberling et al., 2018). This indicates the influence of another
 480 element in the solid solution present in the natural system as Sr or Pb (identified in the colloidal
 481 fractions, see Table 1). Sr in a $(Ra_x, Sr_y, Ba_{1-x-y})SO_4$ solid solution induces a higher partition
 482 coefficient than the $(Ra_x, Ba_{1-x})SO_4$ system (Vinograd et al., 2018; Brandt et al., 2020). Indeed,
 483 colloidal fractions of Sr and Pb were also calculated (see Table 1). PHREEQC modelling of
 484 the equilibrium of a $(Sr_y, Ba_{1-y})SO_4$ solid solution using Guggenheim coefficient from Heberling
 485 et al., 2017 shows that the solutions are in equilibrium with barite solid solutions containing
 486 0.01% Sr. According to Vinograd et al. (2018), this would lead to an increase of D by a factor
 487 of around 3. A $(Ra_x, Pb_z, Ba_{1-x-z})SO_4$ solid solution could also account for the difference in D
 488 (same trend, but weaker influence). Such solid solution systems with three to four end-
 489 members allow for an even better understanding of ^{226}Ra retention in the colloidal fraction of
 490 the water but modelling with a simple $(Ra_x, Ba_{1-x})SO_4$ solid solution is sufficient to reproduce
 491 the colloidal retention of ^{226}Ra .

492 Concurrently, ^{226}Ra sorption on the other minerals observed (kaolinite, smectite, ferrihydrite,
 493 and goethite) was assessed by modelling. Sorption on kaolinite, despite being overestimated
 494 by our choice of attributing all colloidal Al to kaolinite, could account for less than 0.001% of
 495 colloidal ^{226}Ra . The possible influence of a greater amount of smectite than the observed 10%,

496 which has a higher sorption capacity (Cation Exchange Capacity of 80-150 meq/100g versus
497 5-15 meq/100g for kaolinite) was also assessed (Reinoso-Maset and Ly, 2016; Robin et al.,
498 2017). In this case, at most 0.1% of the colloidal ^{226}Ra could be explained by sorption onto
499 montmorillonite. Ferrihydrite accounted for less than 0.4% of colloidal ^{226}Ra for all samples.
500 Goethite, which has lower sorption capacities than ferrihydrite, could not sorb any ^{226}Ra . All
501 these calculations are given in Supplementary Information (Figure SI-9). Retention by barite is
502 thus able to explain the measured colloidal fraction of ^{226}Ra , which is not the case for sorption
503 on iron hydroxides or clay minerals.

504

505 5.2. Uranium retention

506 U is present in the solutions in very low concentrations ($< 50 \text{ nmol/L}$) with less than 65% in
507 colloidal fraction. U sorption was tested on clay minerals and iron oxy-hydroxides according to
508 the modelling described in Figure 1 when colloidal U was measured as well as colloidal Fe (8
509 samples: S2, S3, S4, S7, S8, S9, S11, S17) or Al (6 samples: S2, S3, S7, S11, S15, S17).
510 Figure 5 shows the results of the modelling. It appears that sorption on kaolinite plays only a
511 minimal role in the colloidal transport of U since colloidal clay minerals (kaolinite and smectite)
512 could sorb only between 0% and 7% of U. A significant part of U could sorb on ferrihydrite as
513 UO_2^{+2} cation and UO_2CO_3 and $\text{UO}_2(\text{CO}_3)_2^{-2}$ complexes: between 2% and 81% of U compared
514 to 7% to 65% of U measured in the colloidal fraction. No U retention was calculated on goethite
515 which has a lower retention capacity than ferrihydrite (see Supplementary Information Figure
516 SI-9). A notable part of the colloidal transport of U can then be explained by sorption on
517 ferrihydrite. Additional modelling on smectite and goethite is available in Supplementary
518 Information.

519

520 6. Conclusion

521 The prediction of the long-term evolution of uranium and ^{226}Ra is essential in areas where
522 uranium and radium concentrations are monitored. In this context, the present paper proposes
523 a multidisciplinary and innovative approach to assess the colloidal transport of ^{226}Ra and
524 uranium in a mining environment by using a large amount of field data and detailed
525 characterizations, which were then combined to build a comprehensive geochemical model.
526 In addition, the colloidal fraction was assessed thanks to the application of the DGT technique
527 which has seldom been used in such studies, in particular for ^{226}Ra .

528 The model was able to quantitatively reproduce the ^{226}Ra concentrations in the colloidal
529 fraction, highlighting the preponderant role of barite, although it constitutes a minor mineral,
530 and despite the predominance of kaolinite and ferrihydrite. Barite occurs in tailings both as a
531 mineral inherited from the ore and as a newly formed phase due to the interaction between the
532 barium-bearing minerals contained in the initial ore such as feldspars and the sulfuric acid used
533 during the process of uranium recovery. The involvement of barite in ^{226}Ra retention in tailings
534 has already been highlighted in many environmental monitoring studies of uranium mines (Liu
535 et al., 2006; Chautard et al., 2020) where it controls its mobility. Uranium concentrations in the
536 colloidal fraction were more difficult to reproduce due to its occurrence at very low
537 concentrations in such an environment and its complex truly dissolved chemistry. The
538 environmental survey of metals and radioelements such as uranium and ^{226}Ra is usually
539 performed after simple filtration at $0.45\ \mu\text{m}$, which includes both truly dissolved and colloidal
540 fractions. In this case, the colloidal fraction may generate an overestimation of the dissolved
541 concentrations (Salonen, 1993; Fernandes et al., 1996; Sankhla et al., 2016; Zubova et al.,
542 2020). The original approach developed in this article, combining solid characterization,
543 measurements of total dissolved and colloidal fractions, and geochemical modelling can be
544 applied to both trace and ultra-trace elements.

545

546 **Acknowledgments**

547 The authors would like to thank the staff of COMUF's ORANO Mining subsidiary who made it
548 possible to collect the samples used in this article. This work was funded by the R&D
549 Environment division of ORANO Mining (funding contract 20.124-MN-UNIV POITIERS). The
550 authors acknowledge financial support from the European Union (ERDF) and Région Nouvelle
551 Aquitaine.

552

553 **References**

- 554 Aiken, G.R., Hsu-Kim, H., Ryan, J.N., 2011. Influence of dissolved organic matter on the
555 environmental fate of metals, nanoparticles, and colloids. *Environ. Sci. Technol.* 45,
556 3196–3201. <https://doi.org/10.1021/es103992s>
- 557 Allison, J.D., Brown, D.S., 1995. MINTEQA2/PRODEFA2—A Geochemical Speciation Model
558 and Interactive Preprocessor, in: *Chemical Equilibrium and Reaction Models*, SSSA
559 Special Publications. pp. 241–252. <https://doi.org/10.2136/sssaspecpub42.c12>
- 560 Ames, L.L., McGarrah, J.E., Walker, B.A., Salter, P.F., 1983. Uranium and radium sorption on
561 amorphous ferric oxyhydroxide. *Chem. Geol.* 40, 135–148.
562 [https://doi.org/10.1016/0009-2541\(83\)90095-5](https://doi.org/10.1016/0009-2541(83)90095-5)
- 563 Bachmaf, S., Merkel, B.J., 2011. Sorption of uranium(VI) at the clay mineral–water interface.
564 *Environ. Earth Sci.* 63, 925–934. <https://doi.org/10.1007/s12665-010-0761-6>
- 565 Backhus, D.A., Ryan, J.N., Groher, D.M., MacFarlane, J.K., Gschwend, P.M., 1993. Sampling
566 colloids and colloid-associated contaminants in ground water. *Groundwater* 31, 466–
567 479. <https://doi.org/10.1111/j.1745-6584.1993.tb01849.x>
- 568 Ballini, M., Chautard, C., Nos, J., Phrommavanh, V., Beaucaire, C., Besançon, C., Boizard, A.,
569 Cathelineau, M., Peiffert, C., Vercouter, T., Vors, E., Descostes, M., 2020. A multi-
570 scalar study of the long-term reactivity of uranium mill tailings from Bellezane site
571 (France). *J. Environ. Radioact.* 218, 106–223.
572 <https://doi.org/10.1016/j.jenvrad.2020.106223>
- 573 Besançon, C., Chautard, C., Beaucaire, C., Savoye, S., Sardini, P., Gérard, M., Descostes,
574 M., 2020. The role of barite in the post-mining stabilization of radium-226: A modeling
575 contribution for sequential extractions. *Minerals* 10.
576 <https://doi.org/10.3390/min10060497>
- 577 Bordelet, G., Beaucaire, C., Phrommavanh, V., Descostes, M., 2018. Chemical reactivity of
578 natural peat towards U and Ra. *Chemosphere* 202, 651–660.
579 <https://doi.org/10.1016/j.chemosphere.2018.03.140>
- 580 Brandt, F., Curti, E., Klinkenberg, M., Rozov, K., Bosbach, D., 2015. Replacement of barite by
581 a (Ba,Ra)SO₄ solid solution at close-to-equilibrium conditions: A combined
582 experimental and theoretical study. *Geochim. Cosmochim. Acta* 155, 1–15.
583 <https://doi.org/10.1016/j.gca.2015.01.016>
- 584 Brandt, F., Klinkenberg, M., Poonosamy, J., Bosbach, D., 2020. Recrystallization and uptake
585 of ²²⁶Ra into Ba-rich (Ba,Sr)SO₄ solid solutions. *Minerals* 10.
586 <https://doi.org/10.3390/min10090812>
- 587 Buffle, J., Leppard, G.G., 1995. Characterization of aquatic colloids and macromolecules. 1.
588 Structure and behavior of colloidal material. *Environ. Sci. Technol.* 29, 2169–2175.
589 <https://doi.org/10.1021/es00009a004>
- 590 Chautard, C., Beaucaire, C., Gerard, M., Roy, R., Savoye, S., Descostes, M., 2020.
591 Geochemical characterization of uranium mill tailings (Bois Noirs Limouzat, France)
592 highlighting the U and 226Ra retention. *J. Environ. Radioact.* 218, 106251.
593 <https://doi.org/10.1016/j.jenvrad.2020.106251>
- 594 Claveranne-Lamolère, C., Lespes, G., Dubascoux, S., Aupiais, J., Pointurier, F., Potin-Gautier,
595 M., 2009. Colloidal transport of uranium in soil: Size fractionation and characterization
596 by field-flow fractionation–multi-detection. *J. Chromatogr. A* 1216, 9113–9119.
597 <https://doi.org/10.1016/j.chroma.2009.08.025>
- 598 Cornell, R.M., Schwertmann, U., 2003. *The Iron Oxides: Structure, Properties, Reactions,*
599 *Occurrences and Uses*, 1st ed. Wiley. <https://doi.org/10.1002/3527602097>
- 600 Curie, M., 1911. Radium and the new concepts in chemistry. Nobel Lecture.
- 601 Curti, E., 1999. Coprecipitation of radionuclides with calcite: estimation of partition coefficients
602 based on a review of laboratory investigations and geochemical data. *Appl. Geochem.*
603 14, 433–445. [https://doi.org/10.1016/S0883-2927\(98\)00065-1](https://doi.org/10.1016/S0883-2927(98)00065-1)
- 604 Curti, E., Fujiwara, K., Iijima, K., Tits, J., Cuesta, C., Kitamura, A., Glaus, M.A., Müller, W.,
605 2010. Radium uptake during barite recrystallization at 23±2°C as a function of solution

606 composition: An experimental ^{133}Ba and ^{226}Ra tracer study. *Geochim. Cosmochim.*
607 *Acta* 74, 3553–3570. <https://doi.org/10.1016/j.gca.2010.03.018>

608 Davison, W., 2016. *Diffusive gradients in thin-films for environmental measurements*,
609 Cambridge University Press. ed.

610 Davison, W., Zhang, H., 1994. In situ speciation measurements of trace components in natural
611 waters using thin-film gels. *Nature* 367, 546–548. <https://doi.org/10.1038/367546a0>

612 Déjeant, A., Bourva, L., Sia, R., Galois, L., Calas, G., Phrommavanh, V., Descostes, M., 2014.
613 Field analyses of ^{238}U and ^{226}Ra in two uranium mill tailings piles from Niger using
614 portable HPGe detector. *J. Environ. Radioact.* 137, 105–112.
615 <https://doi.org/10.1016/j.jenvrad.2014.06.012>

616 Déjeant, A., Galois, L., Roy, R., Calas, G., Boekhout, F., Phrommavanh, V., Descostes, M.,
617 2016. Evolution of uranium distribution and speciation in mill tailings, COMINAK Mine,
618 Niger. *Sci. Total Environ.* 545–546, 340–352.
619 <https://doi.org/10.1016/j.scitotenv.2015.12.027>

620 Denaix, L., Semlali, R., Douay, F., 2001. Dissolved and colloidal transport of Cd, Pb, and Zn
621 in a silt loam soil affected by atmospheric industrial deposition. *Environ. Pollut.* 114,
622 29–38. [https://doi.org/10.1016/S0269-7491\(00\)00204-9](https://doi.org/10.1016/S0269-7491(00)00204-9)

623 Doerner, H.A., Hoskins, W.M., 1925. Co-precipitation of radium and barium sulfates. *J Am*
624 *Chem Soc* 47, 662–675. <https://doi.org/10.1021/ja01680a010>

625 Drozdak, J., Leermakers, M., Gao, Y., Phrommavanh, V., Descostes, M., 2015. Evaluation
626 and application of Diffusive Gradients in Thin Films (DGT) technique using Chelex®-
627 100, Metsorb™ and Diphonix® binding phases in uranium mining environments. *Anal.*
628 *Chim. Acta* 889, 71–81. <https://doi.org/10.1016/j.aca.2015.07.057>

629 Drozdak, J., Leermakers, M., Gao, Y., Phrommavanh, V., Descostes, M., 2016. Novel
630 speciation method based on Diffusive Gradients in Thin Films for in situ measurement
631 of uranium in the vicinity of the former uranium mining sites. *Environ. Pollut.* 214, 114–
632 123. <https://doi.org/10.1016/j.envpol.2016.04.004>

633 Dzombak, D.A., Morel, F.M.M., 1990. *Surface Complexation Modelling. Hydrous Ferric Oxide.*
634 John Wiley & Sons.

635 Equeenuddin, S.M., Akhtar, S., Bastia, F., Rout, S.S., Saikia, P.J., 2020. Role of colloid in
636 metal transport in river water around Jaduguda uranium mines, Singhbhum shear zone.
637 *J. Earth Syst. Sci.* 129, 23. <https://doi.org/10.1007/s12040-019-1262-y>

638 Fernandes, H.M., Franklin, M.R., Veiga, L.H.S., Freitas, P., Gomiero, L.A., 1996. Management
639 of uranium mill tailing: Geochemical processes and radiological risk assessment. *J.*
640 *Environ. Radioact.* 30, 69–95. [https://doi.org/10.1016/0265-931X\(95\)00032-6](https://doi.org/10.1016/0265-931X(95)00032-6)

641 Fesenko, S., Carvalho, F., Martin, P., Moore, W., Yankovic, T., 2014. *The environmental*
642 *behaviour of Radium: Revised edition (Technical reports series No. 476).* IAEA,
643 Vienna, Austria.

644 Forsberg, J., Dahlqvist, R., Gelting-Nyström, J., Ingri, J., 2006. Trace metal speciation in
645 brackish water using Diffusive Gradients in Thin Films and ultrafiltration: Comparison
646 of techniques. *Environ. Sci. Technol.* 40, 3901–3905.
647 <https://doi.org/10.1021/es0600781>

648 Glynn, P., 2000. Solid-solution solubilities and thermodynamics: sulfates, carbonates and
649 halides. *Rev. Mineral. Geochem.* 40, 481–511. <https://doi.org/10.2138/rmg.2000.40.10>

650 Gnanapragasam, E.K., Lewis, B.-A.G., 1995. Elastic strain energy and the distribution
651 coefficient of radium in solid solutions with calcium salts. *Geochim. Cosmochim. Acta*
652 59, 5103–5111. [https://doi.org/10.1016/0016-7037\(95\)00356-8](https://doi.org/10.1016/0016-7037(95)00356-8)

653 Grandia, F., Merino, J., Bruno, J., 2008. Assessment of the radium-barium co-precipitation and
654 its potential influence on the solubility of Ra in the near-field (Technical Report No. TR-
655 08-07). Amphos, Swedish Nuclear Fuel and Waste Management Co.

656 Guggenheim, E.A., 1937. The theoretical basis of Raoult's law. *Trans. Faraday Soc.* 33, 151.
657 <https://doi.org/10.1039/TF9373300151>

658 Harguindeguy, S., Crançon, P., Potin Gautier, M., Pointurier, F., Lespes, G., 2019. Colloidal
659 mobilization from soil and transport of uranium in (sub)-surface waters. *Environ. Sci.*
660 *Pollut. Res.* 26, 5294–5304. <https://doi.org/10.1007/s11356-018-2732-5>

661 Heberling, F., Metz, V., Böttle, M., Curti, E., Geckeis, H., 2018. Barite recrystallization in the
662 presence of ^{226}Ra and ^{133}Ba . *Geochim. Cosmochim. Acta* 232, 124–139.
663 <https://doi.org/10.1016/j.gca.2018.04.007>

664 Heberling, F., Schild, D., Degering, D., Schäfer, T., 2017. How well suited are current
665 thermodynamic models to predict or interpret the composition of $(\text{Ba,Sr})\text{SO}_4$ solid-
666 solutions in geothermal scalings? *Geotherm. Energy* 5, 9.
667 <https://doi.org/10.1186/s40517-017-0068-x>

668 Hebert, B., 2018. Approche quantitative par spectrométrie Vis-NIR des minéraux argileux et
669 uranifères dans les sables du gisement de Tortkuduk, Kazakhstan (phdthesis).
670 Université de Poitiers.

671 Husson, A., Leermakers, M., Descostes, M., Lagneau, V., 2019. Environmental geochemistry
672 and bioaccumulation/bioavailability of uranium in a post-mining context – The Bois-
673 Noirs Limouzat mine (France). *Chemosphere* 236, 124341.
674 <https://doi.org/10.1016/j.chemosphere.2019.124341>

675 IAEA, 2004. The long term stabilization of uranium mill tailings (Final report of a co-ordinated
676 research project). Vienna, Austria.

677 IAEA, 2013. Management of NORM Residues (No. IAEA-TECDOC-1712). Vienna, Austria.

678 Javed, M.B., Cuss, C.W., Shotyk, W., 2020. Dissolved versus particulate forms of trace
679 elements in the Athabasca River, upstream and downstream of bitumen mines and
680 upgraders. *Appl. Geochem.* 122, 104706.
681 <https://doi.org/10.1016/j.apgeochem.2020.104706>

682 Kaplan, D.I., Bertsch, P.M., Adriano, D.C., Orlandini, K.A., 1994. Actinide association with
683 groundwater colloids in a coastal plain aquifer. *Radiochim. Acta* 181–187.

684 Kretzschmar, R., Schäfer, T., 2005. Metal retention and transport on colloidal particles in the
685 environment. *Elements* 1, 205–210. <https://doi.org/10.2113/gselements.1.4.205>

686 Lahrouch, F., Baptiste, B., Dardenne, K., Rothe, J., Elkaim, E., Descostes, M., Gerard, M.,
687 2022. Uranium speciation control by uranyl sulfate and phosphate in tailings subject to
688 a Sahelian climate, Cominak, Niger. *Chemosphere* 287, 132139.
689 <https://doi.org/10.1016/j.chemosphere.2021.132139>

690 Lahrouch, F., Guo, N., Hunault, M.O.J.Y., Solari, P.L., Descostes, M., Gerard, M., 2021.
691 Uranium retention on iron oxyhydroxides in post-mining environmental conditions.
692 *Chemosphere* 264, 128473. <https://doi.org/10.1016/j.chemosphere.2020.128473>

693 Landa, E.R., 2004. Uranium mill tailings: nuclear waste and natural laboratory for geochemical
694 and radioecological investigations. *J. Environ. Radioact.* 77, 1–27.
695 <https://doi.org/10.1016/j.jenvrad.2004.01.030>

696 Langmuir, D., Reise, A.C., 1985. The thermodynamic properties of radium. *Geochim
697 Cosmochim Acta* 49, 1593–1601. [https://doi.org/10.1016/0016-7037\(85\)90264-9](https://doi.org/10.1016/0016-7037(85)90264-9)

698 Langmuir, D., Riese, A.C., 1985. The thermodynamic properties of radium. *Geochim.
699 Cosmochim. Acta* 49, 1593–1601. [https://doi.org/10.1016/0016-7037\(85\)90264-9](https://doi.org/10.1016/0016-7037(85)90264-9)

700 Lecomte, A., Michels, R., Cathelineau, M., Morlot, C., Brouand, M., Flotté, N., 2020. Uranium
701 deposits of Franceville basin (Gabon): Role of organic matter and oil cracking on
702 uranium mineralization. *Ore Geol. Rev.* 123, 103579.
703 <https://doi.org/10.1016/j.oregeorev.2020.103579>

704 Leermakers, M., Gao, Y., Navez, J., Poffijn, A., Croes, K., Baeyens, W., 2009. Radium analysis
705 by sector field ICP-MS in combination with the Diffusive Gradients in Thin Films (DGT)
706 technique. *J. Anal. At. Spectrom.* 24, 1115. <https://doi.org/10.1039/b821472g>

707 Leermakers, M., Mbachou, B.E., Husson, A., Lagneau, V., Descostes, M., 2019. An alternative
708 sequential extraction scheme for the determination of trace elements in ferrihydrite rich
709 sediments. *Talanta* 199, 80–88. <https://doi.org/10.1016/j.talanta.2019.02.053>

710 Leermakers, M., Phrommavanh, V., Drozdak, J., Gao, Y., Nos, J., Descostes, M., 2016. DGT
711 as a useful monitoring tool for radionuclides and trace metals in environments impacted
712 by uranium mining: Case study of the Sagnes wetland in France. *Chemosphere* 155,
713 142–151. <https://doi.org/10.1016/j.chemosphere.2016.03.138>

714 Liu, Q., Cui, Z., Etsell, T., 2006. Characterization of Athabasca oil sands froth treatment tailings
715 for heavy mineral recovery. *Fuel* 85, 807–814.
716 <https://doi.org/10.1016/j.fuel.2005.08.032>

717 Loueyit, C.J., Keiffer, B., Fourcade, S., Nzengue, J.C., Bernhard, S., 2002. Study of the post-
718 closure provisions for managing solid tailings from the extraction and processing of
719 uranium ores resulting from the industrial activities of the COMUF company at
720 Mounana, Gabon.

721 Mahoney, J., Cadle, S., Jakubowski, R., 2009. Uranyl adsorption onto hydrous ferric oxides -
722 A re-evaluation for the diffuse layer model database. *Env. Sci Technol* 43, 9260–9266.
723 <https://doi.org/10.1021/es901586w>

724 Martin, A., Crusius, J., Jay McNee, J., Yanful, E., 2003. The mobility of radium-226 and trace
725 metals in pre-oxidized subaqueous uranium mill tailings. *Appl. Geochem.* 18, 1095–
726 1110. [https://doi.org/10.1016/S0883-2927\(02\)00243-3](https://doi.org/10.1016/S0883-2927(02)00243-3)

727 McDevitt, B., McLaughlin, M., Cravotta, C.A., Ajemigbitse, M.A., Van Sice, K.J., Blotevogel, J.,
728 Borch, T., Warner, N.R., 2019. Emerging investigator series: radium accumulation in
729 carbonate river sediments at oil and gas produced water discharges: implications for
730 beneficial use as disposal management. *Environ. Sci. Process. Impacts* 21, 324–338.
731 <https://doi.org/10.1039/C8EM00336J>

732 Michie, U.M., 1979. Evidence for a higher natural uranium content in world rivers. *Nature* 282,
733 112–112. <https://doi.org/10.1038/282112a0>

734 Missana, T., García-Gutiérrez, M., Alonso, Ú., 2004. Kinetics and irreversibility of cesium and
735 uranium sorption onto bentonite colloids in a deep granitic environment. *Appl. Clay Sci.*
736 26, 137–150. <https://doi.org/10.1016/j.clay.2003.09.008>

737 Missana, T., García-Gutiérrez, M., Maffiotte, C., 2003. Experimental and modeling study of the
738 uranium (VI) sorption on goethite. *J. Colloid Interface Sci.* 260, 291–301.
739 [https://doi.org/10.1016/S0021-9797\(02\)00246-1](https://doi.org/10.1016/S0021-9797(02)00246-1)

740 Nirdosh, I., Trembley, W.B., Johnson, C.R., 1990. Adsorption-desorption studies on the
741 226Ra-hydrated metal oxide systems. *Hydrometallurgy* 24, 237–248.
742 [https://doi.org/10.1016/0304-386X\(90\)90089-K](https://doi.org/10.1016/0304-386X(90)90089-K)

743 Nordstrom, D.K., 2011. Hydrogeochemical processes governing the origin, transport and fate
744 of major and trace elements from mine wastes and mineralized rock to surface waters.
745 *Appl. Geochem.* 26, 1777–1791. <https://doi.org/10.1016/j.apgeochem.2011.06.002>

746 Nordstrom, D.K., Blowes, D.W., Ptacek, C.J., 2015. Hydrogeochemistry and microbiology of
747 mine drainage: An update. *Appl. Geochem.* 57, 3–16.
748 <https://doi.org/10.1016/j.apgeochem.2015.02.008>

749 Novotnik, B., Chen, W., Evans, R.D., 2018. Uranium bearing dissolved organic matter in the
750 porewaters of uranium contaminated lake sediments. *Appl. Geochem.* 91, 36–44.
751 <https://doi.org/10.1016/j.apgeochem.2018.01.009>

752 Ouyang, B., Renock, D.J., Ajemigbitse, M. a., Van Sice, K., Warner, N.R., Landisa, J.D., Feng,
753 X., 2019. Radium in hydraulic fracturing wastewater: Distribution in suspended solids
754 and implications to its treatment by sulfate co-precipitation. *Env. Sci Process Impacts*
755 21, 339–351. <https://doi.org/10.1039/c8em00311d>

756 Pagel, M., Somot, S., 2002. Mineralogy and geochemistry of uranium mill tailings. Czech
757 Geological Survey, Czech Republic.

758 Parkhurst, D., Appelo, T., 2013. Description of input and examples for PHREEQC version 3-A
759 computer program for speciation, batch-reaction, one-dimensional transport, and
760 inverse geochemical calculations. *US Geol. Surv. Tech. Methods* 6-A43, 497.

761 Patra, A.C., Sumesh, C.G., Mohapatra, S., Sahoo, S.K., Tripathi, R.M., Puranik, V.D., 2011.
762 Long-term leaching of uranium from different waste matrices. *J. Environ. Manage.* 92,
763 919–925. <https://doi.org/10.1016/j.jenvman.2010.10.046>

764 Phan, T.T., Capo, R.C., Stewart, B.W., Graney, J.R., Johnson, J.D., Sharma, S., Toro, J.,
765 2015. Trace metal distribution and mobility in drill cuttings and produced waters from
766 Marcellus Shale gas extraction: Uranium, arsenic, barium. *Appl. Geochem.* 60, 89–
767 103. <https://doi.org/10.1016/j.apgeochem.2015.01.013>

768 Phrommavanh, V., Leermakers, M., de Boissezon, H., Nos, J., Koko, M.-B., Descostes, M.,
769 2013. Characterizing the Transport of Natural Uranium and its Decay Product ^{226}Ra ,
770 Downstream from Former Mines in France. *Procedia Earth Planet. Sci.* 7, 693–696.
771 <https://doi.org/10.1016/j.proeps.2013.03.064>

772 Porcelli, D., Andersson, P.S., Baskaran, M., Wasserburg, G.J., 2001. Transport of U- and Th-
773 series nuclides in a Baltic shield watershed and the Baltic sea. *Geochim. Cosmochim.*
774 *Acta* 65, 2439–2459. [https://doi.org/10.1016/S0016-7037\(01\)00610-X](https://doi.org/10.1016/S0016-7037(01)00610-X)

775 Reiller, P.E., Descostes, M., 2020. Development and application of the thermodynamic
776 database PRODATA dedicated to the monitoring of mining activities from exploration
777 to remediation. *Chemosphere* 251, 126301.
778 <https://doi.org/10.1016/j.chemosphere.2020.126301>

779 Reinoso-Maset, E., Ly, J., 2014. Study of major ions sorption equilibria to characterize the ion
780 exchange properties of kaolinite. *J Chem Eng Data* 59, 4000–4009.
781 <https://doi.org/10.1021/je5005438>

782 Reinoso-Maset, E., Ly, J., 2016. Study of uranium(VI) and radium(II) sorption at trace level on
783 kaolinite using a multisite ion exchange model. *J. Environ. Radioact.* 157, 136–148.
784 <https://doi.org/10.1016/j.jenvrad.2016.03.014>

785 Robertson, J., Hendry, M.J., Kotzer, T., Hughes, K.A., 2018. Geochemistry of uranium mill
786 tailings in the Athabasca Basin, Saskatchewan, Canada: A review. *Crit. Rev. Environ.*
787 *Sci. Technol.* 49, 1237–1293. <https://doi.org/10.1080/10643389.2019.1571352>

788 Robin, V., Tertre, E., Beaucaire, C., Regnault, O., Descostes, M., 2017. Experimental data and
789 assessment of predictive modeling for radium ion-exchange on beidellite, a swelling
790 clay mineral with a tetrahedral charge. *Appl. Geochem.* 85, 1–9.
791 <https://doi.org/10.1016/j.apgeochem.2017.07.009>

792 Sajih, M., Bryan, N.D., Livens, F.R., Vaughan, D.J., Descostes, M., Phrommavanh, V., Nos,
793 J., Morris, K., 2014. Adsorption of radium and barium on goethite and ferrihydrite: A
794 kinetic and surface complexation modelling study. *Geochim. Cosmochim. Acta* 146,
795 150–163. <https://doi.org/10.1016/j.gca.2014.10.008>

796 Salonen, L., 1993. A rapid method for monitoring of uranium and radium in drinking water. *Sci.*
797 *Total Environ.* 130–131, 23–35. [https://doi.org/10.1016/0048-9697\(93\)90056-C](https://doi.org/10.1016/0048-9697(93)90056-C)

798 Sankhla, M.S., Kumari, M., Nandan, M., Kumar, R., Agrawal, P., 2016. Heavy Metals
799 Contamination in Water and Their Hazardous Effect on Human Health-A Review.
800 *SSRN Electron. J.* <https://doi.org/10.2139/ssrn.3428216>

801 Schlegel, M.L., Descostes, M., 2009. Uranium uptake by hectorite and montmorillonite: a
802 solution chemistry and polarized EXAFS study. *Environ. Sci. Technol.* 43, 8593–8598.
803 <https://doi.org/10.1021/es902001k>

804 Seigneur, N., De Windt, L., Déjeant, A., Lagneau, V., Descostes, M., 2021. Long-Term
805 Evolution of Uranium Mobility within Sulfated Mill Tailings in Arid Regions: A Reactive
806 Transport Study. *Minerals* 11, 1201. <https://doi.org/10.3390/min11111201>

807 Silva, L.F.O., Santosh, M., Schindler, M., Gasparotto, J., Dotto, G.L., Oliveira, M.L.S., Hochella
808 Jr., M.F., 2021. Nanoparticles in fossil and mineral fuel sectors and their impact on
809 environment and human health: A review and perspective. *Gondwana Res.* 92, 184–
810 201. <https://doi.org/10.1016/j.gr.2020.12.026>

811 Soesoo, A., Vind, J., Hade, S., 2020. Uranium and thorium resources of Estonia. *Minerals* 10.
812 <https://doi.org/10.3390/min10090798>

813 Stumm, W., 1997. Reactivity at the mineral-water interface: dissolution and inhibition. *Colloids*
814 *Surf. Physicochem. Eng. Asp.* 120, 143–166. [https://doi.org/10.1016/S0927-7757\(96\)03866-6](https://doi.org/10.1016/S0927-7757(96)03866-6)

815 Sylwester, E., Hudson, E., Allen, P., 2000. The structure of uranium (VI) sorption complexes
816 on silica, alumina, and montmorillonite. *Geochim. Cosmochim. Acta* 64, 2431–2438.
817 [https://doi.org/10.1016/S0016-7037\(00\)00376-8](https://doi.org/10.1016/S0016-7037(00)00376-8)

818 Tayal, A., Conradson, S.D., Kanzari, A., Lahrouch, F., Descostes, M., Gerard, M., 2019.
819 Uranium speciation in weathered granitic waste rock piles: an XAFS investigation. *RSC*
820 *Adv.* 9, 11762–11773. <https://doi.org/10.1039/C9RA00961B>

821

822 Tonello, P.S., Goveia, D., Rosa, A.H., Fraceto, L.F., Menegário, A.A., 2011. Determination of
823 labile inorganic and organic species of Al and Cu in river waters using the diffusive
824 gradients in thin films technique. *Anal. Bioanal. Chem.* 399, 2563–2570.
825 <https://doi.org/10.1007/s00216-010-4603-x>

826 Turrero, M.-J., Gómez, P., del Villar, L.P., Moulin, V., Magonthier, M.-C., Menager, M.-T.,
827 1995. Relation between colloid composition and the environment of their formation:
828 application to the El Berrocal site (Spain). *Appl. Geochem.* 10, 119–131.
829 [https://doi.org/10.1016/0883-2927\(95\)00003-3](https://doi.org/10.1016/0883-2927(95)00003-3)

830 Van Sice, K., Cravotta, C.A., McDevitta, B., Taskera, T.L., Landisc, J.D., Puhra, J., Warnera,
831 N.R., 2018. Radium attenuation and mobilization in stream sediments following oil and
832 gas wastewater disposal in western Pennsylvania. *App Geochem* 98, 393–403.
833 <https://doi.org/10.1016/j.apgeochem.2018.10.011>

834 Vinograd, V.L., Brandt, F., Rozov, K., Klinkenberg, M., Refson, K., Winkler, B., Bosbach, D.,
835 2013. Solid–aqueous equilibrium in the BaSO₄–RaSO₄–H₂O system: First-principles
836 calculations and a thermodynamic assessment. *Geochim. Cosmochim. Acta* 122, 398–
837 417. <https://doi.org/10.1016/j.gca.2013.08.028>

838 Vinograd, V.L., Kulik, D.A., Brandt, F., Klinkenberg, M., Weber, J., Winkler, B., Bosbach, D.,
839 2018. Thermodynamics of the solid solution - Aqueous solution system (Ba,Sr,Ra)SO₄
840 + H₂O: II. Radium retention in barite-type minerals at elevated temperatures. *Appl.*
841 *Geochem.* 93, 190–208. <https://doi.org/10.1016/j.apgeochem.2017.10.019>

842 Wang, Q., Cheng, T., Wu, Y., 2014. Influence of mineral colloids and humic substances on
843 uranium(VI) transport in water-saturated geologic porous media. *J. Contam. Hydrol.*
844 170, 76–85. <https://doi.org/10.1016/j.jconhyd.2014.10.007>

845 Wang, Y., Fruttschi, M., Suvorova, E., Phrommavanh, V., Descostes, M., Osman, A.A.A.,
846 Geipel, G., Bernier-Latmani, R., 2013. Mobile uranium(IV)-bearing colloids in a mining-
847 impacted wetland. *Nat. Commun.* 4, 2942. <https://doi.org/10.1038/ncomms3942>

848 WHO, 2009. WHO Handbook on Indoor Radon: A Public Health Perspective. World Health
849 Organization.

850 Yan, X., Luo, X., 2015. Radionuclides distribution, properties, and microbial diversity of soils
851 in uranium mill tailings from southeastern China. *J. Environ. Radioact.* 139, 85–90.
852 <https://doi.org/10.1016/j.jenvrad.2014.09.019>

853 Yoshida, Y., Yoshikawa, H., Nakanishi, T., 2008. Partition coefficient of Ra and Ba in calcite.
854 *Geochem. J.* 42, 295–304.

855 Závodska, L., Ščerbáková, L., Lesný, J., 2008. Environmental chemistry of uranium.

856 Zhang, H., Davison, W., 1999. Diffusional characteristics of hydrogels used in DGT and DET
857 techniques. *Anal. Chim. Acta* 398, 329–340. [https://doi.org/10.1016/S0003-2670\(99\)00458-4](https://doi.org/10.1016/S0003-2670(99)00458-4)

858

859 Zhang, H., Davison, W., 2000. Direct in situ measurements of labile inorganic and organically
860 bound metal species in synthetic solutions and natural waters using diffusive gradients
861 in thin films. *Anal. Chem.* 72, 4447–4457. <https://doi.org/10.1021/ac0004097>

862 Zubova, E.M., Kashulin, N.A., Dauvalter, V.A., Denisov, D.B., Valkova, S.A., Vandysh, O.I.,
863 Slukovskii, Z.I., Terentyev, P.M., Cherepanov, A.A., 2020. Long-term environmental
864 monitoring in an arctic lake polluted by metals under climate change. *Environments* 7.
865 <https://doi.org/10.3390/environments7050034>

866

867